Atmos. Meas. Tech. Discuss., 8, 8817–8857, 2015
www.atmos-meas-tech-discuss.net/8/8817/2015/
doi:10.5194/amtd-8-8817-2015

Atmospheric Measurement Techniques Discussions
Open Access

The uncertainty of the atmospheric integrated water vapour estimated from GNSS observations

T. Ning[1,2], J. Wang[3], G. Elgered[1], G. Dick[2], J. Wickert[2], M. Bradke[2], and M. Sommer[4]

[1]Department of Earth and Space Sciences, Chalmers University of Technology, Onsala Space Observatory, 43992 Onsala, Sweden
[2]Section GPS/Galileo Earth Observation, Helmholtz-Zentrum Potsdam, Deutsches GeoForschungsZentrum (GFZ), Telegrafenberg, 14473 Potsdam, Germany
[3]Department of Atmospheric and Environmental Sciences, University at Albany, SUNY, Albany, NY, USA
[4]Richard-Aßmann-Observatorium, Deutscher Wetterdienst, Lindenberg, Germany

Received: 10 August 2015 – Accepted: 14 August 2015 – Published: 27 August 2015

Correspondence to: T. Ning (tongn@gfz-potsdam.de)

Published by Copernicus Publications on behalf of the European Geosciences Union.

Abstract

Within the Global Climate Observing System (GCOS) Reference Upper Air Network (GRUAN) there is a need for an assessment of the uncertainty in the Integrated Water Vapour (IWV) in the atmosphere estimated from ground-based GNSS observations. All relevant error sources in GNSS-derived IWV is therefore essential to be investigated. We present two approaches, a statistical and a theoretical analysis, for the assessment of the uncertainty of the IWV. It will be implemented to the GNSS IWV data stream for GRUAN in order to obtain a specific uncertainty for each data point. In addition, specific recommendations are made to GRUAN on hardware, software, and data processing practices to minimize the IWV uncertainty. By combining the uncertainties associated with the input variables in the estimations of the IWV, we calculated the IWV uncertainties for several GRUAN sites with different weather conditions. The results show a similar relative importance of all uncertainty contributions where the uncertainties in the Zenith Total Delay (ZTD) dominate the error budget of the IWV contributing with over 75 % to the total IWV uncertainty. The impact of the uncertainty associated with the conversion factor between the IWV and the Zenith Wet Delay (ZWD) is proportional to the amount of water vapour and increases slightly for moist weather conditions. The GRUAN GNSS IWV uncertainty data will provide a quantified confidence to be used for the validation of other measurement techniques, taking the uncertainty into account from diurnal to decadal time scales.

1 Introduction

In the hydrological cycle, water vapour is an important variable for transferring heat energy from the Earth's surface to its atmosphere and in moving heat around the Earth. Meanwhile, water vapour is a very important greenhouse gas due to its ability of absorbing long wave thermal radiation emitted from the Earth's surface. Hence, the atmospheric water vapour is very important for the Earth's climate system and its variability is a key to understand the hydrological cycle. A variety of systems exist for measuring the atmospheric integrated water vapour (IWV), e.g., radiosondes (Ross and Elliott, 1996), microwave radiometry (Elgered, 1993), Very Long Baseline Interferometry (VLBI) (Heinkelmann et al., 2007), and Global Navigation Satellite Systems (GNSS) (Bevis et al., 1992). Standing out from others, GNSS observations from the ground can be made under in principle all weather conditions with a high temporal resolution (a few minutes), and its spatial resolution is continuously improving when more continuously operating stations are installed. Therefore, using ground-based GNSS measurements to derive IWV has drawn a lot of scientific attention and has been investigated (e.g., Wang et al., 2007; Vey et al., 2010; Ning et al., 2013). In order to interpret GNSS measurements correctly and draw valid conclusions on the quality of the resulting IWV estimates, the uncertainty of the GNSS-derived IWV must be carefully evaluated and quantified.

The procedure for the estimation of the atmospheric IWV from GNSS measurements begins with the propagation delay of the GNSS signals when passing through the Earth's neutral atmosphere. The propagation delay can be estimated in the GNSS data processing, together with other parameters such as coordinates, as a Zenith Total Delay (ZTD) which is separated into two parts: the Zenith Hydrostatic Delay (ZHD) and the Zenith Wet Delay (ZWD). The ZHD can be determined from surface pressure measurements (Davis et al., 1985) and the ZWD depends on the amount of water vapour in the column of air, i.e., the IWV, through which the signal passes and can be estimated from the data themselves.

All GNSS measurements are subject to error sources that influence the uncertainty of the estimated ZTD. The accuracy of the ZHD depends on the accuracy of the ground pressure. Additionally, the conversion from the ZWD to the IWV will add uncertainties, e.g., due to imperfect determination of the mean temperature of the atmosphere. All those uncertainties shall be included when we calculate the final uncertainty of the GNSS-derived IWV. Errors in GNSS measurements can be random or systematic, or more commonly a mixture of both, depending on the time scale studied. Since the ex-

AMTD
8, 8817–8857, 2015

pected (mean) value of random errors is zero, the impact of such errors is reduced as the number of measurements increases. Systematic errors cannot be averaged out as the length of measurements becomes longer. They can however change at a specific time epoch. For example, a change of the GNSS antenna or its environment may introduce such an offset. Systematic errors may also change slowly with time, e.g., the impact of signal multipath at a GNSS site may vary due to growing vegetation (Pierdicca et al., 2014).

Depending on different applications, the requirement on the accuracy of the estimated IWV varies. For forecasting application the demand is mainly the timing and approximate IWV of moving air masses while the accuracy of individual IWV estimate and the IWV biases is of less importance. Therefore, less accurate real time orbit estimation can be used in forecasting applications. For climate research, it is crucial to have a high accuracy with as small biases as possible in order to obtain the absolute value over long time scale. In this case, final GNSS orbit estimation with the highest accuracy is necessary. The focus of this study is to discuss and assess the accuracy of the IWV derived from ground-based GNSS measurements obtained from post processed data and mainly used for climate research.

Many studies have investigated the uncertainty of the GNSS-derived IWV either by comparing the GNSS IWV with data obtained from other independent techniques, e.g., Pacione et al. (2002) and Rózsa (2014), or by combining the uncertainties of the input variables used in order to obtain the uncertainty of the GNSS IWV, (e.g., Wang et al., 2007; Ning et al., 2013; Van Malderen et al., 2014). In order to conduct a complete and comprehensive investigation on the uncertainty of the GNSS IWV, the two methods are both discussed in this study in order to develop a method which is applicable to each individual data point. The uncertainty method will be implemented to the GNSS IWV data stream for GCOS (Global Climate Observing System) Reference Upper Air Network (GRUAN). The objectives of GRUAN are to provide long-term, high-quality upper-air climate records, to constrain/calibrate data from more spatially-comprehensive global observing systems (including satellites), and to measure a large suite of co-related cli-

AMTD
8, 8817–8857, 2015

mate variables (Seidel et al., 2009). One of the most important objectives of GRUAN is to collect reference observations. Each GRUAN reference observation is required to provide a comprehensive uncertainty analysis (Immler et al., 2010). Ground-based GNSS IWV was identified as a priority 1 measurement for GRUAN. This study is intended to develop methods to calculate GNSS IWV uncertainties for each data point and to work with the GRUAN GNSS central data processing centre (GFZ) to incorporate them into the GRUAN GNSS data stream.

The paper is structured as follows. Sections 2 and 3 discuss the two uncertainty analyses: a statistical and a theoretical one. A sequence of subsections is given in Section 3 in order to describe each of the errors which contributes to the final total uncertainty of the GNSS-derived IWV. In the last subsection, the individual error sources are then summarized into an overall error budget in order to obtain the final uncertainty of the GNSS-derived IWV. The conclusions are given in Sect. 4.

2 Statistical analysis

A statistical analysis (Moses, 1986) can be used to evaluate the uncertainty of the GNSS-derived IWV if independent estimates are available from at least three co-located techniques, measuring the same true variability of the IWV. The individual IWV estimates from techniques *A* and *B* are expressed as:

$$V_{A(i)} = V_i + M_A + \varepsilon_{A(i)}, \quad (1)$$

$$V_{B(i)} = V_i + M_B + \varepsilon_{B(i)}, \quad (2)$$

where V_i is the true value of the IWV for the epoch i; M_A and M_B are the biases (the systematic error) for each technique, respectively; $\varepsilon_{A(i)}$ and $\varepsilon_{B(i)}$ are the random errors. The observed Standard Deviation (SD) of the IWV difference between techniques *A* and B based on N simultaneously sampled data points can be expressed as:

$$S_{A-B} = \sqrt{\frac{1}{N-1}\sum_{i=1}^{N}\left(V_{A(i)} - V_{B(i)} - (\overline{V_A} - \overline{V_B})\right)^2}, \quad (3)$$

where the overline denotes the mean value. From Eqs. (1) and (2) we have:

$$\overline{V_A} = \overline{V} + M_A + \overline{\varepsilon_A}, \quad (4)$$

$$\overline{V_B} = \overline{V} + M_B + \overline{\varepsilon_B}, \quad (5)$$

where $\overline{V}$ is the mean value of the true IWV. If we combine Eqs. (1), (2), (4), and (5) with Eq. (3), we get:

$$S_{A-B} = \sqrt{\frac{1}{N-1}\sum_{i=1}^{N}\left(\varepsilon_{A(i)} - \varepsilon_{B(i)} - \overline{\varepsilon_A} + \overline{\varepsilon_B}\right)^2}. \quad (6)$$

For a long time period of measurements giving a zero mean of random errors ($\overline{\varepsilon_A}=\overline{\varepsilon_B}=0$), and assuming that ε_A and ε_B are uncorrelated, Eq. (6) can be expressed as:

$$S_{A-B} = \sqrt{\overline{\varepsilon_A^2} + \overline{\varepsilon_B^2}}, \quad (7)$$

where the ε terms can be solved by forming the equation above three times for pairwise comparisons using the three techniques.

Since the ε terms only address the random errors, in order to determine the total uncertainty of the IWV, caused by both random and systematic errors, the biases (M_A and M_B) for two techniques also need to be derived. The mean IWV difference between

AMTD
8, 8817–8857, 2015

two techniques is expressed as:

$$\frac{1}{N}\sum_{i=1}^{N}\left(V_{A(i)} - V_{B(i)}\right)$$
$$= \frac{1}{N}\sum_{i=1}^{N}\left(V_{(i)} + M_A + \varepsilon_{A(i)} - V_{(i)} - M_B - \varepsilon_{B(i)}\right)$$
$$= M_A + \overline{\varepsilon_A} - M_B - \overline{\varepsilon_B}, \qquad (8)$$

where the output of Eq. (8) is highly depending on the length of time scale of measurements studied. For a short time period where the length of measurements is not long enough to average out random errors, Eq. (8) gives a mixture of random and systematic errors. For a long time period giving a zero mean of random errors, the equation gives $M_A - M_B$.

From Eq. (8), for a long time period of measurements, the IWV bias (M) for one technique can only be obtained when it is compared to a technique with a known IWV bias or no bias at all. After obtaining the values for both ε and M, the total uncertainty of the IWV can be determined:

$$\sigma_V = \sqrt{\overline{\varepsilon^2} + M^2}. \qquad (9)$$

One example of statistical analyses can be found in Ning et al. (2012). The authors presented the results from comparisons of 10-year-long time series of ZWD, estimated using GNSS, geodetic VLBI, and a water vapour radiometer (WVR). These three techniques are co-located at the Onsala Space Observatory separated by less than 100 m. Since the VLBI antenna has a very high directivity, the VLBI-derived ZWD is not affected by signal multipath. Meanwhile, there was no instrument changes occurring on the Onsala VLBI antenna for the last 30 years. Therefore, the VLBI-derived ZWD for the 10-year-long time period can be considered as having only a small constant bias. Using Eqs. (7)–(9), we calculated total uncertainties in the ZWD and in the corresponding

AMTD
8, 8817–8857, 2015

IWV, for each technique after assuming a bias of +2, 0 and −2 mm in the VLBI-derived ZWD. The results are summarized in Table 1 where depending on the assumed VLBI bias, the uncertainties for the GNSS-derived IWV are around 0.5, 0.7, and 1 kg m^{-2}, respectively.

Since all known biases must be removed before derivation of the uncertainty, an assumption is made about no bias in an other measurement technique. For most of the GRAUN sites, measurements simultaneously acquired from at least three co-located independent techniques are difficult. In this case, the next approach to calculate GNSS-derived IWV uncertainty is more useful.

3 Theoretical analysis

A theoretical analysis is desired, where the total uncertainty of the GNSS-derived IWV (σ_V) is calculated from the uncertainties associated with the input variables according to the rule of uncertainty propagation for uncorrelated input quantities. The equation used for a theoretical analysis is (Immler et al., 2010):

$$\sigma_V = \sqrt{\sum_{i=1}^{M} \left(\frac{\partial f(v_1, \ldots, v_M)}{\partial v_i} \sigma_i \right)^2}, \tag{10}$$

where $f(v_1, \ldots, v_M)$ is the functional relationship between the GNSS-derived IWV and the input variables; σ_i is the one sigma uncertainty of the corresponding variable.

The GNSS-derived IWV is converted from the ZWD via the conversion factor Q

$$V = \frac{\ell_w^z}{Q}, \tag{11}$$

where the ZWD is given by the subtraction of the ZHD from the ZTD:

$$\ell_w^z = \ell_t^z - \ell_h^z. \tag{12}$$

AMTD
8, 8817–8857, 2015

Combination of Eqs. (11) and (12) gives the functional relationship:

$$V = \frac{\ell_t^z - \ell_h^z}{Q}. \quad (13)$$

Insertion of Eq. (13) into Eq. (10) gives the expression for the propagation of the uncertainties from different sources to the total IWV uncertainty:

$$\sigma_V = \sqrt{\left(\frac{\sigma_{\mathrm{ZTD}}}{Q}\right)^2 + \left(\frac{\sigma_{\mathrm{ZHD}}}{Q}\right)^2 + \left(V\frac{\sigma_Q}{Q}\right)^2}. \quad (14)$$

In order to calculate σ_V, we first need to study and determine values for Q, σ_{ZTD}, σ_{ZHD}, and σ_Q.

3.1 Error budget of the GNSS-derived ZTD

The fundamental observable of the GNSS technique is the propagation time of a signal, transmitted from the GNSS satellites, passing through the Earth's atmosphere to the receivers (ground-based). When we consider the error budget of the GNSS-derived ZTD, errors from several parts need to be taken into account which will be discussed in this section.

3.1.1 GNSS satellite orbits

Errors in the estimates of the satellite coordinates will propagate directly to the estimates of the GNSS parameters. If we use the Precise Point Positioning (PPP) strategy to process the data obtained from a permanent GNSS site where the site coordinates are usually kept fixed (one estimate per day), eliminate the ionosphere delay to the first order, and use the final clock product from the International GNSS Service (IGS), the orbit error is compensated by ZTD, receiver clock and ambiguity parameters (Douša, 2010):

$$\cos \Psi_A^{\prime i} \sigma_{X_{\mathrm{Rad}}^i} + \sin \Psi_A^{\prime i} \sigma_{X_{\mathrm{Tan}}^i} = \frac{1}{\cos z_A^{\prime i}} \sigma_{\mathrm{ZTD}} + \sigma_{T_A} + \lambda_f \sigma_{N_i} \tag{15}$$

with

$$\Psi_A^{\prime i} = \arcsin(\sin z_A^{\prime i} R_A / R^i), \tag{16}$$

where $z_A^{\prime i}$ is the zenith angle seen from the ground receiver A to the satellite i; R_A and R^i are the distances from the top of the receiver to the geocentre, and the geometrical distance from the satellite to the geocentre, respectively; $\sigma_{X_{\mathrm{Rad}}^i}$ and $\sigma_{X_{\mathrm{Tan}}^i}$ are the radial and the tangential (along-track + cross-track) orbit errors. σ_{ZTD} is the ZTD error; σ_{T_A} is the receiver clock error and σ_{N_i} is the ambiguity error. Based on Eq. (15), Fig. 1 depicts the impact of different components of the orbit errors on the estimated ZTD as the function of zenith angle and the impact factor indicates how the ZTD error correlates with the orbit error. It is evident that the radial orbit error dominates the resulting ZTD error and the maximum impact occurs when the satellite is in the zenith direction. The maximum impact factor due to the tangential orbit errors is 0.13 and is observed at a zenith angle of 45°

Figure 1 was produced by ignoring the parts for the receiver clock error and the ambiguity error in Eq. (15) and by assuming that the estimated ZTD compensate all the radial and tangential orbit errors. In order to determine how much of the orbit errors that will be mapped into the estimated ZTD when the two other parameters (receiver clock and ambiguity) are estimated, we carried out simulations for three GRUAN sites. These are LDBO (14.1° E, 52.2° N), LDRZ (169.7° E, −45.0° N), and NYA2 (11.9° E, 78.9° N). We first processed the GPS data for the year 2014 using a PPP strategy. For each site, we calculated satellite-receiver range based on the estimated site coordinate and the satellite coordinates provided by IGS for each epoch where the corresponding estimated ZTD and receiver clock error from the PPP processing are added back to the calculated range together with known ambiguities. Finally, for each satellite-receiver range we added the range error projected from the corresponding orbit error which was calculated by the left part of Eq. (15). The ZTD, receiver clock, and the ambiguity parameters were estimated again using PPP and compared to the old PPP solution in order to determine how the orbits errors map to the different estimated parameters.

Table 2 (taken from http://igscb.jpl.nasa.gov/mail/igsmail/2010/msg00001.html) presents the orbit accuracy for each component using the IGS reprocessed orbit product, which should be comparable to the operational final orbits. The mean and standard deviation were calculated based on satellite position repeatability for each pair of consecutive days. For the simulation, we used constants 15 and 38 mm for the radial and the tangential (square root of along and cross) orbit errors, respectively.

Figure 2 depicts results for the three GRUAN sites where the ZTD errors from the simulation for one day (1 June 2014) are plotted along with two other theoretical ZTD errors. One is calculated by Eq. (15) but only taking the radial orbit errors into account and assuming that all orbit errors are compensated by the ZTD. The other was calculated in the same way but only taking the tangential orbit errors into account. The results indicate that most portion of the orbit errors (> 90 %) are compensated by other two parameters (receiver clock and ambiguity) and the mean simulated ZTD errors vary from 1.5 to 3 mm. In addition, the simulated ZTD errors show a higher correlation (~ 0.60) to the theoretical ZTD errors caused by the radial orbit errors than the one caused by the tangential orbit errors. The larger uncertainties, seen for the site LDB0 and after the hour 15, are caused both by the larger radial orbit errors and by a worse geometry of the satellites (less number of satellites visible). Similar results are seen (not shown) if we perform the simulation for one year of data for the three sites. The mean ZTD simulated errors are around 3 mm for the sites LDB0 and LDRZ while the one for the site NYA2 is 1.5 mm. The corresponding standard deviations are around 1 and 0.4 mm, respectively.

AMTD
8, 8817–8857, 2015

3.1.2 Ionospheric delay

The Earth's ionosphere contains electrons in sufficient quantity to significantly delay the propagation of GNSS signals. The ionospheric delay is dependent on the total amount of free electrons along the propagation path, named Total Electron Content (TEC), and the carrier frequency of GNSS signals. Normally, in order to remove the ionospheric impact, an ionosphere-free linear combination is used:

$$\Phi_{\text{ion\_free}} = \frac{f_1^2}{f_1^2 - f_2^2}\Phi_1 - \frac{f_2^2}{f_1^2 - f_2^2}\Phi_2, \tag{17}$$

where Φ_1 and Φ_2 are carrier phase measurements from two different frequencies (e.g., L1 and L2 for GPS). Since this virtual measurement can only eliminate the ionospheric delay to the first order ($\sim$ 99.9 % of the total delay), smaller contributions from higher order terms remain, which however have more dramatic impact during strong solar activities, e.g., ionospheric storms (Pireaux et al., 2010).

Fritsche et al. (2005) carried out an investigation on the impact of including corrections of the ionospheric delay for higher-order terms on GNSS estimates using a global network, and with a focus on the solar maximum between 2001 and 2003. The authors found a linear dependency between the difference in the estimated vertical position and the peak electron densities (varying approximately from 2 to 12 mm when the daily means of the TEC unit increase from 25 to 175) when no corrections were applied for 2nd and 3rd-order terms. The ZTD difference is approximately a factor of three smaller than the vertical position difference (Hill et al., 2009). The corresponding ZTD difference is then from 0.6 to 4 mm. This is consistent to the result reported by Fritsche et al. (2005) where a $\sim$ 2 mm difference in the ZTD were observed when the TEC unit (a TEC unit equals $10^1 6$ electons m^{-2}) reaches 150. However, over long time periods the impact on average values are less. A study was performed by Petrie et al. (2010) for the time period from 1995 to 2008. Using approximately 60 globally distributed GNSS sites, they found that the mean difference in the vertical component, after applying 2nd

AMTD
8, 8817–8857, 2015

and 3rd-order terms, was in the range from −0.3 to 0.5 mm (corresponding to the ZTD difference from −0.1 to 0.2 mm) for sites with data spanning at least 10 years. The result indicates that the impact on the ZTD from the higher-order terms is insignificant over a long time series.

3.1.3 Signal multipath

Differences in the ZTD caused by signal multipath depend strongly on the elevation angle of the observation and is different from site to site due to a changing electromagnetic environment. In order to demonstrate the impact of multipath effects, we carried out analyses using different elevation cutoff angles in the PPP data processing for three GRUAN sites (LDB0, LDRZ, and NYA2) together with two other sites: LDB2 (14.1° E, 52.2° N) and POTS (13.1° E, 52.4° N). One month of GPS data acquired from June 2014 were processed using four different elevation cutoff angles: 5, 10, 15, and 20°. We calculated the monthly mean of the estimated ZTD for each solution relative to the value from the solution using a 5° cutoff angle. The results are shown in Fig. 3 where the most significant elevation dependent ZTD difference is seen for the site LDB0 while the least is given by the site LDRZ. The results indicate that the impact of multipath effects is highly site dependent. This is further examined by the two co-located sites: LDB0 and LDB2 that are both located at Richard Aßmann Observatory of the German Weather Service, Lindenberg, Germany with a baseline less than 100 m. The photographs of the two sites are given in Fig. 4. The two sites use two different antennas. The one used for LDB2 is LEICA25 which is choke ring antenna while the one used for LDB0 is a JAV_GRANT_G3T (www.ngs.noaa.gov/ANTCAL/main.jsp). The choke ring antennas are designed to reduce multipath signals. The result for LDB2 shows less multipath effects than the one for LDB0 (see Fig. 4). However, the vertical metal rod beside the LDB2 may cause multipath while the flat surface below the antenna may also cause systematic effects. Furthermore, the LDB2 antenna is covered by a plastic radome which may also introduce elevation dependent impacts (see discussion in next section).

AMTD
8, 8817–8857, 2015

A similar investigation on the multipath effects was carried out by Ning et al. (2011) using GNSS sites at the Onsala Space Observatory. Using nearly 80 days of GNSS data they found an IWV difference of 1.7 mm (corresponding to ∼ 11 mm in ZTD) between a 5° solution and a 20° solution. Such difference can be significantly reduced by using microwave absorbing material, e.g., ECCOSORB®, attached below the antenna plane.

Signal multipath is highly dependent on the local environment and it can vary in time, e.g., due to changes in soil moisture (Larson et al., 2010) and growing vegetation (Pierdicca et al., 2014). Therefore, it is difficult to have a general model to quantify the multipath effect on the estimated ZTD. For all GRUAN GNSS sites, a microwave absorbing material, such as ECCOSORB, is highly recommended to be installed to the antenna in order to minimize the impact of the multipath effects.

3.1.4 Antenna related errors

In order to obtain the highest accuracy in the ZTD estimates, antenna related errors, i.e., Phase Centre Variations (PCV) and radome effects, need to be removed. Therefore, an absolute calibration of the PCV for all the GNSS satellite transmitting antennas and the ground antenna (Schmid et al., 2007) is necessary to be implemented in the GNSS data processing. The difference in the ZTD estimated with and without applying the PCV correction can vary from 2 to 10 mm (Byun and Bar-Sever, 2009; Thomas et al., 2011). Nowadays PCV corrections are normally always applied in order to eliminate this error source.

To avoid the accumulation of snow and for a general protection, many GNSS antennas are equipped with radomes. Different shapes of radomes yield different impacts on the phase of the GNSS signal. Emardson et al. (2000) found that the IWV offset introduced by a conical shaped radome can be up to 1 mm (about 6.5 mm in ZTD). A smaller impact (less than 2 mm in ZTD) was observed by Ning et al. (2011) from the use of a hemispheric radome which is recommended if a GRUAN GNSS site is going to install a radome. Ning et al. (2011) also found that the impact of the radome depends

AMTD
8, 8817–8857, 2015

on the different geometries of the electromagnetic environment of the antenna, as well as with the elevation cutoff angle for the observations used in the analysis. Therefore, applying a radome calibration in the data processing is necessary in order to reduce the radome impacts. This is done by using calibration tables provided and updated by IGS which include a set of calibrations for a particular antenna and for a particular radome.

3.1.5 Mapping functions

In GNSS data processing, the slant path delay is converted to the equivalent ZTD (sum of the ZHD and the ZWD) using Mapping Functions (MFs):

$$\ell_t^z = m_\mathrm{h}(\epsilon) \cdot \ell_\mathrm{h}^z + m_\mathrm{w}(\epsilon) \cdot \ell_\mathrm{w}^z, \tag{18}$$

where ϵ is the elevation angle seen from the ground receiver to the satellite; m_h and m_w are the hydrostatic and the wet mapping functions, respectively. Stoew et al. (2007) evaluated the accuracy of the New Mapping Functions (NMF) (Niell, 1996) and the Improved Mapping Functions (IMF) (Niell, 2000) using radiosonde data. The resulting mean (M) and standard deviation (σ) of the slant delay errors were modeled by:

$$M(\epsilon) = M_0 \cdot e^{-\epsilon/\epsilon_M}, \tag{19}$$

$$\sigma(\epsilon) = \sigma_0 \cdot e^{-\epsilon/\epsilon_\sigma}. \tag{20}$$

Values calculated from Eqs. (19) and (20) for four elevation angles (5, 7, 10, and 15°) are summarized in Table 3. It is clear that the accuracy of MFs is highly elevation dependent and the MF induced errors on slant delays are insignificant when the elevation angle is getting larger.

Currently the most popular and accurate MF is the Vienna Mapping Function 1 (VMF1) since it can capture the short-term variability of the atmosphere by utilizing data from a numerical weather model (Boehm et al., 2006). Zus et al. (2015) carried out an investigation on the accuracy of the VMF1 by comparing a MF called GFZ-VMF1, which is based on the VMF1 concept, with a direct mapping approach. They found that if a GPS site is located 2 km above the MF model orography and if a low elevation is used (3°), the error on the estimated vertical component can be up to 1 cm (corresponding to approximately 3 mm in ZTD). They also pointed out that it is difficult to distinguish the MF-caused error from a variety of other errors presented at the low elevation angles, e.g, poor or missing antenna PCV models and multipath. Given this fact, for the GRUAN data products, instead of quantifying the ZTD uncertainty from the applied MF, we may choose a slightly higher elevation cutoff angle, i.e., > 10°, for the GPS data processing in order to significantly reduce the MF induced error.

3.1.6 Summary of the ZTD uncertainty

All GRUAN GNSS data will be processed by the German Research Centre for Geosciences (GFZ) using GFZ's inhouse GNSS software package, Earth Parameter and Orbit determination System (EPOS) (Deng, 2012) where only the PPP approach will be implemented in the data processing. The formal error, provided for each time epoch by the estimation process of PPP, is only dependent on the amount of carrier phase measurements and the constellation of the satellites for a given site (Byun and Bar-Sever, 2009). In order to take systematic errors in the GPS orbit into account, the method discussed in Sect. 3.1.1 will be applied and the calculated ZTD error for each time epoch will be added to the corresponding formal error. In addition, in order to reduce the ZTD uncertainty due to other factors, i.e., the ones discussed in Sects. 3.1.2–3.1.5, following conditions need to be fulfilled in the GPS data processing:

- corrections for the 2nd order of the ionospheric delay are applied,
- final orbit/clock products from IGS or equivalent are used,

AMTD
8, 8817–8857, 2015

- absolute satellite and ground antenna PCV models and radome calibrations are implemented; a hemispheric radome and an ECCOSORB plate are recommended,
- signal multipath effects need to be minimized either by implementing microwave absorbing material to the antenna, or by locating the GNSS antenna in an favorable place,
- use an elevation cutoff angle of 10° or higher. A higher elevation cutoff angle will degrade the geometry and increase the formal error of the ZTD estimate. However, this may still be desired for applications where long-term trends are estimated and systematic errors such as signal multipath rather than formal errors are the limiting factor (Ning and Elgered, 2012).

The procedure to determine the total ZTD uncertainty for each time epoch is described as follows. For each GRUAN site, the daily GPS data will be processed first using a PPP strategy in order to obtain the ZTD estimates and corresponding formal errors together with receiver clock errors. Thereafter, the estimated ZTD and receiver clock errors will be used in a simulation in order to estimate the ZTD errors due to the orbit errors. Then the root sum square (RSS) of the simulated ZTD error and the corresponding formal error gives total ZTD uncertainty for each time epoch. Figure 5 depicts the estimated ZTD for one day (1 June 2014) for three GRUAN sites together with the corresponding calculated total ZTD uncertainty for each time epoch (5 min). The results show that the daily mean ZTD uncertainty is 3.8 mm for the site LDB0 while the values for the sites LDRZ and NYA2 are 3.7 and 3.0 mm, respectively. The result also indicates that the ZTD uncertainty is not correlated with the magnitude of the ZTD. These values are consistent to the claimed 1-σ uncertainty (4 mm) by IGS's final ZTD product.

AMTD
8, 8817–8857, 2015

3.2 Uncertainty of the ZHD

The ZHD for a given GNSS site can be calculated using the ground pressure

$$\ell_h^z = (2.2767 \pm 0.0015)\,\frac{P_0}{f(\lambda,H)}, \tag{21}$$

where the constant 2.2767 is calculated from the refractivity of dry air, the universal gas constant, and an effective value of the acceleration due to gravity at the site (Bevis et al., 1994). The resulting uncertainty includes the different contributions which are assumed to be uncorrelated. In Eq. (21), ZHD is in units of mm, P_0 in hPa, and

$$f(\lambda,H) = \left(1 - 2.66\cdot 10^{-3}\cos(2\lambda) - 2.8\cdot 10^{-7}H\right), \tag{22}$$

where λ and H are the site latitude in degrees and the height above the geoid in m, respectively. The expression $f(\lambda,H)$ is used to model the variation of the acceleration due to gravity in the ZHD. An example, for different latitudes and heights, is shown in Fig. 6. The uncertainties in the latitude and the height are negligible. The uncertainty of the ZHD is mainly determined by the uncertainty in the ground pressure (σ_{P_0}) and the uncertainty of the constant (σ_c). Using Eq. (10), we have the uncertainty of the ZHD in mm:

$$\sigma_{\mathrm{ZHD}} = \sqrt{\left(\frac{2.2767\,\sigma_{P_0}}{f(\lambda,H)}\right)^2 + \left(\frac{P_0\,\sigma_c}{f(\lambda,H)}\right)^2}. \tag{23}$$

All GRUAN sites should be equipped with surface barometers which provide accuracies much better than 0.5 hPa. One example is shown in Fig. 7 which depicts the pressure differences between three barometers at the Onsala Space Observatory, Sweden. The barometer from the Swedish Meteorological and Hydrological Institute (SMHI) was used as reference. The absolute accuracy of the SMHI barometer is better than 0.2 hPa. It has been calibrated approximately every second year. Additionally the SMHI barometer is traceable to the SI unit within 0.1 hPa. The small annual variations observed from the Setra barometer are likely due to a sensor sensitivity to the temperature. The uncertainty of surface pressure measured by GRUAN barometers will be estimated using uncertainty estimation protocols presented in Immler et al. (2010). It will be used to estimate the ZHD uncertainty using Eq. (23).

For the GNSS sites which are not equipped with barometers, other methods have been investigated. Wang et al. (2007) found an average RMS difference of 1.7 hPa given by comparisons between the ground pressure interpolated, both spatially and temporally, from nearby surface synoptic observations and local ground measurements at 48 globally distributed GNSS sites covering a 8 year time period. Similar comparisons were carried out by Heise et al. (2009), but using the interpolated ground pressure from the ECMWF meteorological analysis at more than 60 global GNSS sites. Using one year of data, they obtained a better agreement with an overall mean bias and a standard deviation of 0.0 and 0.9 hPa, respectively. We did a similar test, but only for the GNSS site at the Onsala Space Observatory, using over 14 years of data. The result shows a mean bias and a standard deviation of 0.1 and 0.6 hPa, respectively. It should be pointed out here that if we use the ground pressure obtained from numerical models interpolated to the height of the GNSS site, the uncertainty of the GNSS height will have an impact on the derived ZHD. Snajdrova et al. (2005) found that 10 m of height difference approximately causes a difference of 3 mm in the ZHD.

3.3 Uncertainty of the conversion factor Q

The conversion factor Q is defined by

$$Q = 10^{-6}\rho_{\mathrm{w}}R_{\mathrm{w}}\left(k_2' + \frac{k_3}{T_{\mathrm{m}}}\right), \tag{24}$$

AMTD
8, 8817–8857, 2015

where ρ_w is the density of liquid water; R_w is the specific gas constant for water vapour; the values of k_3 and k_2' can be estimated from laboratory experiments; T_m is a mean temperature.

In Eq. (24), the uncertainties of the density of liquid water (ρ_w) and the specific gas constant for water vapour (R_w) are 0.002 kg m^{-3} (Wolf, 2008) and 0.008 J (kg·K)$^{-1}$ (http://physics.nist.gov/cuu/Constants/index.html), respectively. Since the impact of the uncertainties from these two parameters is insignificant (less than 0.1 % of the total Q uncertainty), the uncertainty of Q is determined by the uncertainties in T_m, k_3, and k_2'. The combination Eqs. (24) and (10) gives:

$$\sigma_Q = 10^{-6}\rho_w R_w \sqrt{\left(\frac{\sigma_{k_3}}{T_m}\right)^2 + \sigma_{k_2'}^2 + \left(k_3\frac{\sigma_{T_m}}{T_m^2}\right)^2}. \tag{25}$$

In order to evaluate the impact of the uncertainty in each variable on the total uncertainty of Q, we need to specify values and uncertainties for the constants k_3 and k_2', which are taken from Bevis et al. (1994). Figure 8 depicts the uncertainty of Q as a function of the uncertainty in T_m assuming that the value of T_m is 279 K. Three groups of values were used for the uncertainties of the constants k_3 and k_2', the nominal value (given by Table 1 in Bevis et al., 1994), the double of the nominal value and the half of nominal the value. It is evident that when the uncertainty of T_m is sufficiently large, it tends to dominate the uncertainty of Q. Furthermore, the uncertainty of k_3 has a larger impact compared to the uncertainty of k_2'.

The parameter T_m can be calculated from the vertical profile of water vapour pressure (p_w) and the physical temperature (T):

$$\int_S \frac{p_w(s)}{T(s)}\,ds = T_m \int_S \frac{p_w(s)}{T(s)^2}\,ds. \tag{26}$$

Globally, T_m can be derived from Numerical Weather Prediction (NWP) models. An RMS difference of 1.3 K in T_m was claimed by Wang et al. (2005) based on global comparisons between the NCEP/NCAR reanalysis and the radiosonde measurements using 6 years of data (NCEP: National Centers for Environmental Prediction of the US weather service; NCAR: National Center for Atmospheric Research). The authors also found a better agreement (1.1 K) in T_m obtained from the ECMWF reanalysis product.

Due to the fact that the ECMWF data provides a temporal resolution of 6 h and a horizontal resolution of about 50 km and there is normally a difference between the model height and the GPS height, a temporal, horizontal and vertical interpolation of the ECMWF data to the time and position of the GPS site is necessary. Details for the interpolation of the ECMWF data can be found in Heise et al. (2009) which are summarized as follows. For the horizontal interpolation the ECMWF interpolation library (EMOSLIB, http://www.ecmwf.int) was used. The 6-hourly ECMWF data were linearly interpolated to the temporal resolution of the GPS ZTD (1 h). The strategy used for the vertical interpolation depends on whether the GPS height is above or below the lowest ECMWF level. For the first case, the temperature and specific humidity of ECMWF were linearly interpolated while pressure was logarithmically interpolated to the GPS height. For the latter case, the temperature was extrapolated using the mean temperature gradient of the three lowest ECMWF layers. The pressure was calculated by stepwise application of the barometric height formula for each 20 m while the specific humidity is estimated in parallel assuming the mean relative humidity from the two lowest ECMWF levels.

3.4 Summary of the uncertainty of the GNSS-derived IWV

We now can calculate the total uncertainty of the GNSS-derived IWV after substituting Eqs. (23) and (25) to Eq. (14):

$$\sigma_V = \sqrt{\left(\frac{\sigma_{\mathrm{ZTD}}}{Q}\right)^2 + \left(\frac{2.2767\,\sigma_{P_0}}{f(\lambda,H)Q}\right)^2 + \left(\frac{P_0\,\sigma_c}{f(\lambda,H)Q}\right)^2 + \left(V\,\frac{\sigma_Q}{Q}\right)^2}. \quad (27)$$

AMTD
8, 8817–8857, 2015

The uncertainty of the GNSS-derived IWV

T. Ning et al.

Table 4 summarizes the calculated total uncertainties of the GNSS-derived IWV for three GRUAN sites: LDBO (14.1° E, 52.2° N), LDRZ (169.7° E, −45.0° N), and NYA2 (11.9° E, 78.9° N). For each site, the GPS data acquired from the year 2014 were processed using a PPP strategy to obtain ZTD time series. The corresponding total ZTD uncertainties were then determined using the approach discussed in Sect. 3.1.6 and the mean values over the year were used. The estimated ZTD were converted to the IWV using the measured ground pressure and the mean temperature obtained from the ECMWF reanalysis data (ERA-Interim). The values of the conversion factor Q were calculated using Eq. (24). In Table 4, the corresponding absolute values for IWV, ZTD, ground pressure, and mean temperature are given using the mean values of the year 2014 for each site.

As shown in Table 4, the uncertainties in the ZTD dominate the error budget of the resulting IWV contributing with over 75 % to the total IWV uncertainty. The impact of the uncertainty associated with the conversion factor Q increases slightly when the weather conditions are getting moist.

The IWV uncertainty is calculated for each data point in the GRUAN data products. Therefore, we first calculated the time series of the total ZTD uncertainty using the method discussed in Sect. 3.1.1. Thereafter, the uncertainties for the ZHD and the conversion factor Q were determined using the uncertainties listed in Table 4 for each input variable. Finally, the total IWV uncertainty was calculated using Eq. (27). One example of the calculated total IWV uncertainties is shown in Fig. 9 for the month of June 2014. The mean IWV uncertainties are 0.68, 0.65, and 0.538 $\mathrm{kg\,m^{-2}}$ for LDB0, LDRZ, and NYA2, respectively. The corresponding variations of IWV uncertainties, given by the standard deviations, are 0.16, 0.13, and 0.068 $\mathrm{kg\,m^{-2}}$. As expected, the variation in the IWV uncertainties are highly correlated to the variation in the ZTD uncertainties and the larger uncertainties, as discussed in Sect. 3.1.1, are caused both by the larger radial orbit errors and by a worse geometry of the satellites (less number of satellites visible).

As discussed above, currently the total IWV uncertainty obtained from a theoretical analysis is calculated by ignoring the site dependent effects, i.e., signal multipath. If the GRUAN site is co-located with other techniques the total IWV uncertainty can be estimated from the statistical method. One example is seen for the IGS station ONSA at the Onsala Space Observatory. The mean total uncertainty obtained from the theoretical analysis is 0.598 $kg\,m^{-2}$ while the uncertainty, given by a statistical analysis, presented in Table 1 is 0.7 $kg\,m^{-2}$ when assuming no bias in the VLBI data. We interpret the difference to be mainly due to site dependent effects ignored in the theoretical analysis.

4 Conclusions

Two methods were discussed in order to determine the total uncertainty of the GNSS-derived IWV. When there are at least three co-located techniques available, measuring the variability of the IWV at the same time, a statistical analysis is applied. This method is, however, difficult to apply on the present observational network because three independent methods for IWV measurement are not available. Therefore, a theoretical analysis, where the total uncertainty of the IWV is calculated from each one of the input variables according to the rule of uncertainty propagation for uncorrelated errors, is used.

In order to minimize the ZTD uncertainty caused by the factors discussed in Sects. 3.1.2–3.1.5, some conditions (see Sect. 3.1.6) need to be fulfilled in the GPS data processing. The method discussed in Sect. 3.1.1 was applied to calculate the ZTD errors caused by the orbit errors for each time epoch which were added to the corresponding formal error. The calculated total ZTD uncertainties for three GRUAN sites are at the same level as the 1-σ ZTD uncertainty (4 mm) calculated by the IGS. The uncertainty of the total IWV is dominated by the uncertainties in the ZTD which contributes with more than 75 % to the total IWV uncertainty.

The theoretical method will be implemented in the GRUAN GNSS central data processing. In summary, the following steps will be taken to calculate IWV uncertainty for each data point. Firstly, the ZTD uncertainty, including the systematic satellite orbit error and the formal error, is calculated. Secondly, the ZHD uncertainty is obtained using the uncertainty of ground pressure, estimated using the method presented by Immler et al. (2010), and the uncertainty in Eq. (21). Thirdly, the uncertainty for the conversion factor Q is calculated using the uncertainties of the mean temperature, k_3, and k_2' listed in Table 4. Finally, the total IWV uncertainty for each data point is calculated using the uncertainties for the ZTD, the ZHD, and the conversion factor Q using Eq. (27).

For sites where two additional independent techniques are available, the IWV uncertainty estimated from the statistical method can be used to assess the stability of the data quality and potentially improve the operational theoretical method. For example, the statistical method can be used to quantify the ZTD uncertainty which may change due to site dependent effects such as signal multipath.

Acknowledgement. This research was supported by Deutscher Wetterdienst through the project "Development of a data product for the GNSS integrated precipitable water vapor column (IPW) following the requirements of the Guide for the GCOS Reference Upper Air Network (GRUAN)".

The article processing charges for this open-access publication were covered by a Research Centre of the Helmholtz Association.

References

Bevis, M., Businger, S., Herring, T., Rocken, C., Anthes, R., and Wave, R.: GPS meteorology: remote sensing of atmospheric water vapor using the global positioning system, J. Geophys. Res., 97, 787–801, doi:10.1029/92JD01517, 1992. 8819

Bevis, M., Chiswell, S., Herring, T. A., Anthes, R. A., Rocken, C., and Ware, R. H.: GPS meteorology: Mapping zenith wet delays onto precipitable water, J. Appl. Meteorol., 33, 379–386, doi:10.1175/1520-0450(1994)033<0379:GMMZWD>2.0.CO;2, 1994. 8834, 8836, 8848

Boehm, J., Werl, B., and Schuh, H.: Troposphere mapping functions for GPS and very long baseline interferometry from European Centre for Medium-Range Weather Forecasts oper-

AMTD

8, 8817–8857, 2015

The uncertainty of the GNSS-derived IWV

T. Ning et al.

ational analysis data, J. Geophys. Res., 111, B02406, doi:10.1029/2005JB003629, 2006. 8831

Byun, S. and Bar-Sever, Y.: A new type of troposphere zenith path delay product of the international GNSS service, J. Geod., 83, 367–373, doi:10.1007/s00190-008-0288-8, 2009. 8830, 8832

Davis, J. L., Herring, T. A., Shapiro, I. I., Rogers, A. E. E., and Elgered, G.: Geodesy by radio interferometry: Effects of atmospheric modelling errors on estimates of baseline length, Radio Sci., 20, 1593–1607, doi:10.1029/RS020i006p01593, 1985. 8819

Deng, Z.: GPS meteoroglogy with signal frequency receivers, PhD Thesis, (Scientific Technical Report; 12/09), Potsdam: Deutsches GeoForschungsZentrum GFZ, Germany, IV, 110 pp., doi:10.2312/GFZ.b103-12099, 2012. 8832

Douša, J.: The impact of errors in predicted GPS orbits on zenith troposphere delay estimation, GPS Solut., 14, 229–239, doi:10.1007/s10291-009-0138-z, 2010. 8825

Elgered, G.: Tropospheric radio path delay from ground-based microwave radiometry, in: Atmospheric Remote Sensing By Microwave Radiometry, Wiley & Sons Inc, New York, USA, 215–258, 1993. 8819

Emardson, T. R., Johansson, J. M., and Elgered, G.: The systematic behavior of water vapor estimates using four years of GPS observations, Trans. IEEE Geosci. Remote Sens., 38, 324–329, doi:10.1109/36.823927, 2000. 8830

Fritsche, M., Dietrich, R., Knöfel, C., Rülke, A., and Vey, S.: Impact of higher-order ionospheric terms on GPS estimates, Geophys. Res. Lett., 32, L23311, doi:10.1029/2005GL024342, 2005. 8828

Hagemann, S., Bengtsson, L., and Gendt, G.: On the determination of atmospheric water vapor from GPS measurements, J. Geophys. Res., 108, 4678, doi:10.1029/2002JD003235, 2003.

Heinkelmann, R., Schmidt, M., Böhm, J., and Schuh, H.: Determination of water vapor trends from VLBI observations, Österreichische Zeitschrift für Vermessung und Geoinformation, 95, 73–79, 2007. 8819

Heise, S., Dick, G., Gendt, G., Schmidt, T., and Wickert, J.: Integrated water vapor from IGS ground-based GPS observations: initial results from a global 5-min data set, Ann. Geophys., 27, 2851–2859, doi:10.5194/angeo-27-2851-2009, 2009. 8835, 8837

Hill, E. M., Davis, J. L., Elósegui, P., Wernicke, B. P., Malikowski, E., and Niemi, N. A.: Characterization of site-specific GPS errors using a short-baseline network of braced

monuments at Yucca Mountain, southern Nevada, J. Geophys. Res., 114, B11402, doi:10.1029/2008JB006027, 2009. 8828
Immler, F. J., Dykema, J., Gardiner, T., Whiteman, D. N., Thorne, P. W., and Vömel, H.: Reference Quality Upper-Air Measurements: guidance for developing GRUAN data products, Atmos. Meas. Tech., 3, 1217–1231, doi:10.5194/amt-3-1217-2010, 2010 8821, 8824, 8835, 8840
Larson, K. M., Braun, J. J., Small, E. E., Zavorotny, V. U., Gutmann, E. D., and Bilich, A. L.: GPS multipath and its relation to near-surface soil moisture content, IEEE J-STARS, 3, 91–99, doi:10.1109/JSTARS.2009.2033612, 2010. 8830
Moses, L. E.: Think and Explain with Statistics, Addison-Wesley, Boston, USA, ISBN 978-0-201-15619-5, 1–3, 1986. 8821
Niell, A.: Global mapping functions for the atmosphere delay at radio wavelengths, J. Geophys. Res., 101, 3227–3246, 1996. 8831
Niell, A.: Improved atmospheric mapping functions for VLBI and GPS, Earth Planets Space, 52, 699–702, doi:10.1029/95JB03048, 2000. 8831
Ning, T., Elgered, G., and Johansson, J. M.: The impact of microwave absorber and radome geometries on GNSS measurements of station coordinates and atmospheric water vapour, Adv. Space. Res., 47, 186–196, doi:10.1016/j.asr.2010.06.023, 2011. 8830
Ning, T., Haas, R., Elgered, G., and Willén, U.: Multi-technique comparisons of ten years of wet delay estimates on the west coast of Sweden, J. Geod., 86, 565–575, doi:10.1007/s00190-011-0527-2, 2012. 8823, 8845
Ning, T. and Elgered, G.: Trends in the atmospheric water vapor content from ground-based GPS: the impact of the elevation cutoff angle, IEEE J-STARS, 5, 744–751, doi:10.1109/JSTARS.2012.2191392, 2012. 8833
Ning, T., Elgered, G., Willén, U., and Johansson, J. M.: Evaluation of the atmospheric water vapor content in a regional climate model using ground-based GPS measurements, J. Geophys. Res.-Atmos., 118, 329–339, doi:10.1029/2012JD018053, 2013. 8819, 8820
Petrie, E. J., King, M. A., Moore, P., and Lavallée, D. A.: Higher-order ionospheric effects on the GPS reference frame and velocities, J. Geophys. Res.-Sol. Ea., 115, B03471, doi:10.1029/2009JB006677, 2010. 8828
Pacione, R., Fionda, E., Ferrara, R., Lanotte, R., Sciarretta, C., and Vespe, F.: Comparison of atmospheric parameters derived from GPS, VLBI and a ground-based microwave radiometer in Italy, Phys. Chem. Earth., 27, 309–316, doi:10.1016/S1474-7065(02)00005-0, 2002. 8820

AMTD
8, 8817–8857, 2015

The uncertainty of the GNSS-derived IWV

T. Ning et al.

Pierdicca, N., Guerriero, L., Giusto, R., Broioni, M., and Egido, A.: SAVERS: A Simulator of GNSS Reflections From Bare and Vegetated Soils, IEEE Trans. Geosci. Remote Sensing, 52, 6542–6554 , doi:10.1109/TGRS.2013.2297572, 2014. 8820, 8830

Pireaux, S., Defraigne, P., Wauters, L., Bergeot, N., Baire, Q., and Bruyninx, C.: Higher-order ionospheric effects in GPS time and frequency transfer, GPS Solut., 14, 267–277, doi:10.1007/s10291-009-0152-1, 2010. 8828

Rothacher, M.: Estimation of station heights with GPS, in: Vertical reference systems, edited by: Drewes, H., Dodson, A., Fortes, L., Sanchez, L., and Sandoval, P., Springer, IAG Symposium Cartagena, Colombia, 20–23 February 2001, 81–90, doi:10.1007/978-662-04683-8_17, 2001.

Rózsa, S.: Uncertainty considerations for the comparison of water vapour derived from radiosondes and GNSS, Proceedings of the IAG General Assembly, Melbourne, Australia, 28 June–2 July 2011, 139, 65–78, doi:10.1007/978-3-642-37222-3_9, 2014. 8820

Ross, R. J. and Elliott, W. P.: Tropospheric water vapor climatology and trends over north America: 1973–93, J. Climate, 9, 3561–3574, doi:10.1175/1520-0442(1996)009<3561:TWVCAT>2.0.CO;2, 1996. 8819

Schmid, R., Steigenberger, P., Gendt, G., Ge, M., and Rothacher, M.: Generation of a consistent absolute phase center correction model for GPS receiver and satellite antennas, J. Geod., 81, 781–798, doi:10.1007/s00190-007-0148-y, 2007. 8830

Seidel, D. J., Berger, F. H., Immler, F., Sommer, M., Vömel, H., Diamond, H. J., Dykema, J., Goodrich, D., Murray, W., Peterson, T., Sisterson, D., Thorne, P., and Wang, J.: Reference upper-air observations for climate: Rationale, progress, and plans, B. Am. Meteorol. Soc., 90, 361–369, doi:10.1175/2008BAMS2540.1, 2009. 8821

Snajdrova, K., Boehm, J., Willis, P., Haas, R., and Schuh, H.: Multi-technique comparison of tropospheric zenith delays derived during the CONT02 campaign, J. Geod., 79, 613–623, doi:10.1007/s00190-005-0010-z, 2005. 8835

Stoew, B., Nilsson, T., Elgered, G., and Jarlemark, P. O. J.: Temporal correlations of atmospheric mapping function errors in GPS estimation, J. Geod., 81, 311–323, doi:10.1007/s00190-006-0114-0, 2007. 8831, 8847

Thomas, I. D., King, M. A., Clarke, P. J., and Penna, N. T.: Precipitable water vapor estimates from homogeneously reprocessed GPS data: An intertechnique comparison in Antarctica, J. Geophys. Res., 116, D04107, doi:10.1029/2010JD013889, 2011. 8830

Van Malderen, R., Brenot, H., Pottiaux, E., Beirle, S., Hermans, C., De Mazière, M., Wagner, T., De Backer, H., and Bruyninx, C.: A multi-site intercomparison of integrated water vapour observations for climate change analysis, Atmos. Meas. Tech., 7, 2487–2512, doi:10.5194/amt-7-2487-2014, 2014. 8820

Vey, S., Dietrich, R., Rülke, A., Fritsche, M., Steigenberger, P., and Rothacher, M.: Validation of Precipitable Water Vapor within the NCEP/DOE Reanalysis Using Global GPS Observations from One Decade, J. Climate, 23, 1675–1695, doi:10.1175/2009JCLI2787.1, 2010. 8819

Wang, J., Zhang, L., and Dai, A.: Global estimates of water-vapor-weighted mean temperature of the atmosphere for GPS applications, J. Geophys. Res.-Atmos., 110, D21101, doi:10.1029/2005JD006215, 2005. 8836, 8848

Wang, J., Zhang, L., Dai, A., Hove, T. V., and Baelen, J. V.: A near-global: 2-hourly data set of atmospheric precipitable water from ground-based GPS measurement, J. Geophys. Res.-Atmos., 112, D11107, doi:10.1029/2006JD007529, 2007. 8819, 8820, 8835

Wolf, H.: Determination of water density: limitations at the uncertainty level of 1×10^{-6}, Accred. Qual. Assur., 13, 587–591, doi:10.1007/s00769-008-0442-2, 2008. 8836

Zus, F., Dick, G., Dousa, J., and Wickert, J.: Systematic errors of mapping functions which are based on the VMF1 concept, GPS Solut., 19, 277–286, doi:10.1007/s10291-014-0386-4, 2015. 8831

AMTD

8, 8817–8857, 2015

The uncertainty of the GNSS-derived IWV

T. Ning et al.

Table 1. ZWD and corresponding IWV uncertainties given by a statistical analysis using observations from Onsala on the Swedish west coast.

	Standard deviation[a] [mm]			Mean difference[a] [mm]			E_{ZWD}[b]	B_{ZWD}[c]	σ_{ZWD}[d]	σ_{V1}[e]	σ_{V2}[f]
	GNSS	VLBI	WVR	GNSS	VLBI	WVR	[mm]	[mm]	[mm]	[kg m^{-2}]	[kg m^{-2}]
VLBI absolute offset 2.0											
GNSS	–	5.1	6.2	–	−3.4	−0.3	3.0	−1.4	3.3	0.51	0.52
VLBI	5.1	–	6.8	3.4	–	3.1	4.1	**2.0**[g]	4.6	0.70	0.71
WVR	6.2	6.8	–	0.3	−3.1	–	5.4	−1.1	5.5	0.85	0.86
VLBI absolute offset 0.0											
GNSS	–	5.1	6.2	–	−3.4	−0.3	3.0	−3.4	4.5	0.70	0.71
VLBI	5.1	–	6.8	3.4	–	3.1	4.1	**0.0**[g]	4.1	0.63	0.64
WVR	6.2	6.8	–	0.3	−3.1	–	5.4	−3.1	6.2	0.96	0.97
VLBI absolute offset −2.0											
GNSS	–	5.1	6.2	–	−3.4	−0.3	3.0	−5.4	6.2	0.95	0.96
VLBI	5.1	–	6.8	3.4	–	3.1	4.1	**−2.0**[g]	4.6	0.70	0.71
WVR	6.2	6.8	–	0.3	−3.1	–	5.4	−5.1	7.4	1.14	1.15

[a] The corresponding values were taken from Table 2 (synchronization to all data) in Ning et al. (2012). [b] The uncertainty of the ZWD only addressing the random errors. [c] The bias in the ZWD estimates for each technique. [d] The total uncertainty of the ZWD addressing both the random and systematic errors. [e] The uncertainty of the IWV given by dividing σ_{ZWD} by 6.5 (a mean value of the conversion factor Q, given by radiosonde measurements, for the Swedish west coast). The uncertainty of Q was neglected. [f] The uncertainty of the IWV calculated using a similar way as σ_{V1}, but taking the uncertainty of 0.1 kg m^{-2} for Q, into account ($\sigma_{V2} = \sqrt{\sigma_{V1}^2 + 0.1^2}$). The uncertainty of the ground pressure is insignificant since the ground measurements, accurate to ±0.1 hPa, were used. [g] Assumed values in order to relate the comparisons to an absolute scale.

AMTD
8, 8817–8857, 2015

Title Page
Abstract | Introduction
Conclusions | References
Tables | Figures
◂◂ | ▸▸
◂ | ▸
Back | Close
Full Screen / Esc
Printer-friendly Version
Interactive Discussion

Table 2. Accuracy of IGS reprocessed orbits for one day[*].

	Along Track [mm]	Cross Track [mm]	Radial [mm]
Mean	−0.2	−1.2	0.4
Standard deviation	26.0	27.2	15.1

[*] Since the day-boundary differences computed in the table from IGSMail (http://igscb.jpl.nasa.gov/mail/igsmail/2010/msg00001.html) involve orbits for two consecutive days, the inferred orbit uncertainty for a single day should be smaller by $\sqrt{2}$ which is presented here.

AMTD
8, 8817–8857, 2015

Table 3. Mean and standard deviation (σ) of the slant delay errors*.

	NMF_h		NMF_w		IMF_h		IMF_w	
Elevation angle	Mean [mm]	σ [mm]	Mean [mm]	σ [mm]	Mean [mm]	σ [mm]	Mean [mm]	σ [mm]
5°	10.6	24.87	−3.3	3.91	1.0	13.68	−2.5	1.87
7°	3.5	9.60	−1.0	1.20	0.4	4.50	−0.8	0.65
10°	0.7	2.30	−0.2	0.21	0.1	0.85	−0.1	0.13
15°	0.0	0.21	−0.0	0.01	0.0	0.05	−0.0	0.00

* Corresponding values for M_0, σ_0, ϵ_M, and ϵ_σ used in Eqs. (19) and (20) were taken from Table 1 in Stoew et al. (2007).

AMTD
8, 8817–8857, 2015

AMTD
8, 8817–8857, 2015

The uncertainty of the GNSS-derived IWV

T. Ning et al.

Title Page
Abstract | Introduction
Conclusions | References
Tables | Figures
Back | Close
Full Screen / Esc
Printer-friendly Version
Interactive Discussion

Table 4. Uncertainties in the GNSS-derived IWV calculated from the uncertainties associated with input variables.

Input variable	LDB0	LDRZ	NYA2	Uncertainty	Corresponding IWV uncertainty LDB0 [$kg\,m^{-2}$]	LDB0 [%]	LDB0 [%][e]	LDRZ [$kg\,m^{-2}$]	LDRZ [%]	LDRZ [%][e]	NYA2 [$kg\,m^{-2}$]	NYA2 [%]	NYA2 [%][e]
ZTD [mm]	2487	2376	2434	3.8, 3.7, 3.3[a]	0.59	1.8	79.9	0.58	2.2	82.2	0.49	2.1	77.0
Ground pressure													
P_0 [hPa]	1000.1	968.7	1005.6	0.2[b]	0.07	0.2	1.2	0.07	0.3	1.3	0.07	0.3	1.5
Constant[f]	2.2767	2.2767	2.2767	0.0015	0.23	0.7	12.2	0.22	0.9	11.9	0.23	1.0	17.0
Mean temperature													
T_m [K]	274.6	270.8	262.3	1.1[c]	0.13	0.4	3.8	0.1	0.4	2.5	0.09	0.4	2.6
k_2' [$K\,hPa^{-1}$]	22.1	22.1	22.1	2.2[d]	0.05	0.2	0.6	0.04	0.2	0.5	0.03	0.2	0.3
k_3 [$10^5 \times K^2\,hPa^{-1}$]	3.739	3.739	3.739	0.012[d]	0.10	0.3	2.3	0.08	0.3	1.6	0.07	0.3	1.6
IWV [$kg\,m^{-2}$]	33	26	23										
Conversion factor Q	6.4	6.5	6.7										
Total IWV uncertainty					0.66	2.0		0.64	2.4		0.56	2.4	

[a] The values are given by the mean ZTD uncertainty calculated from one year of data for LDB0, LDRZ, and NYA2, respectively. [b] For GRUAN sites equipped with surface barometers which are calibrated routinely. [c] Taken from Wang et al. (2005) based on the comparison between ECMWF reanalysis and radiosonde data. [d] Taken from Table 1 in Bevis et al. (1994). [e] Percentage of the total IWV uncertainty. [f] The constant given in Eq. (21).

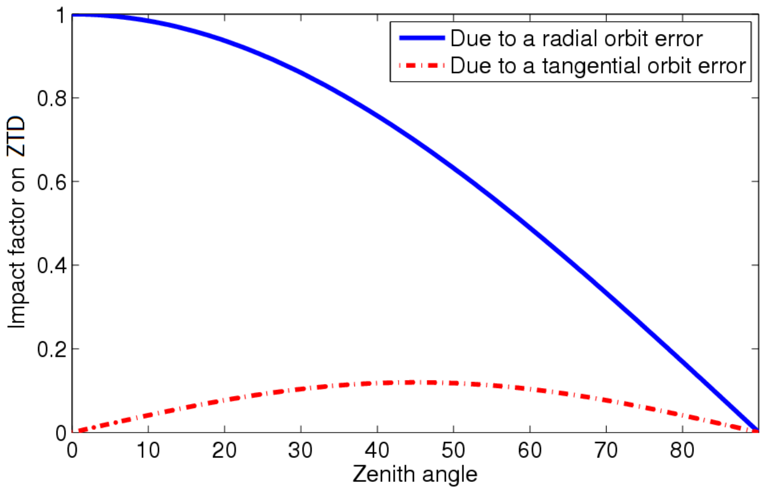

Figure 1. The impact of the radial and the tangential orbit errors in the estimated ZTD.

AMTD
8, 8817–8857, 2015

The uncertainty of the GNSS-derived IWV

T. Ning et al.

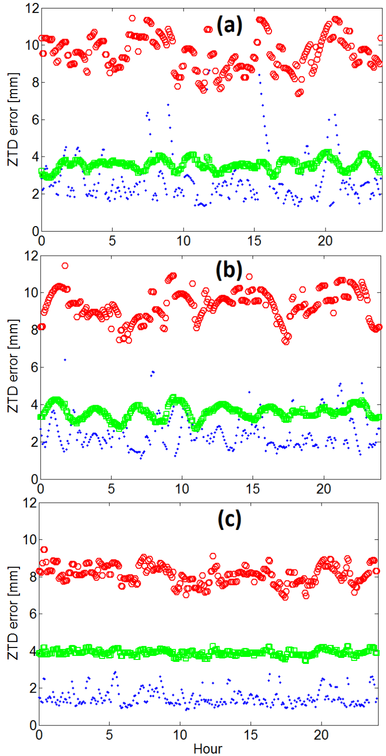

Figure 2. The ZTD error due to orbit errors for three GRUAN sites: **(a)** LDB0, **(b)** LDRZ and **(c)** NYA2, where the blue dots show the simulated ZTD error, the red circles show the theoretical ZTD error caused only by the radial orbit error, and the green squares show the theoretical ZTD error caused only by the tangential orbit error.

AMTD
8, 8817–8857, 2015

The uncertainty of the GNSS-derived IWV

T. Ning et al.

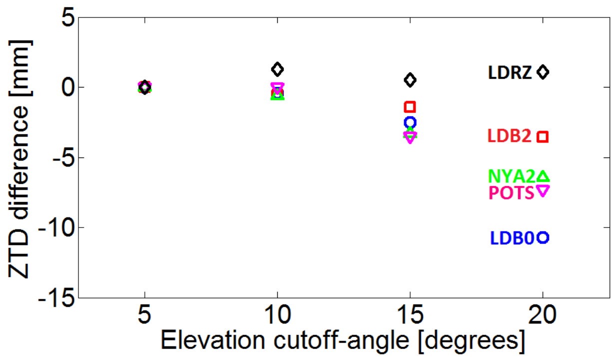

Figure 3. The impact of the elevation cutoff angle on the estimated ZTD for five GRUAN sites. The result obtained from the 5° elevation cutoff solution is used as the reference which however does not necessarily mean that it is the most accurate. Ideally, if all models are correct the result shall not depend on the cutoff angle at all.

AMTD
8, 8817–8857, 2015

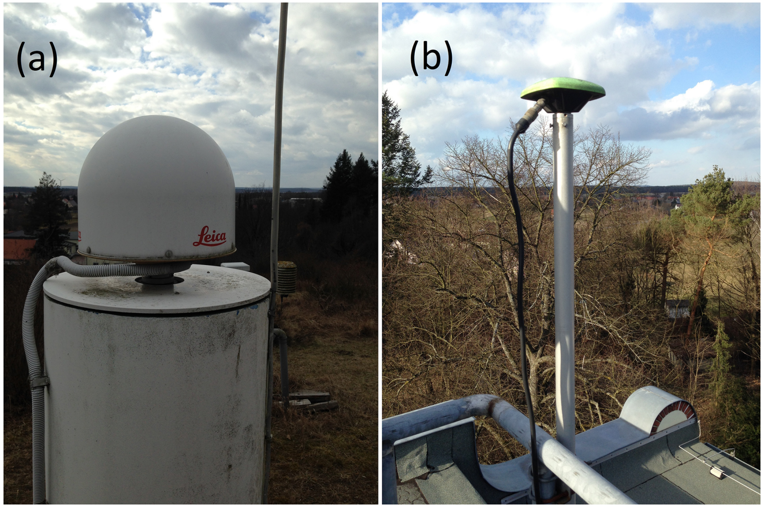

Figure 4. Photographs of two GRUAN sites: **(a)** LDB2 and **(b)** LDB0.

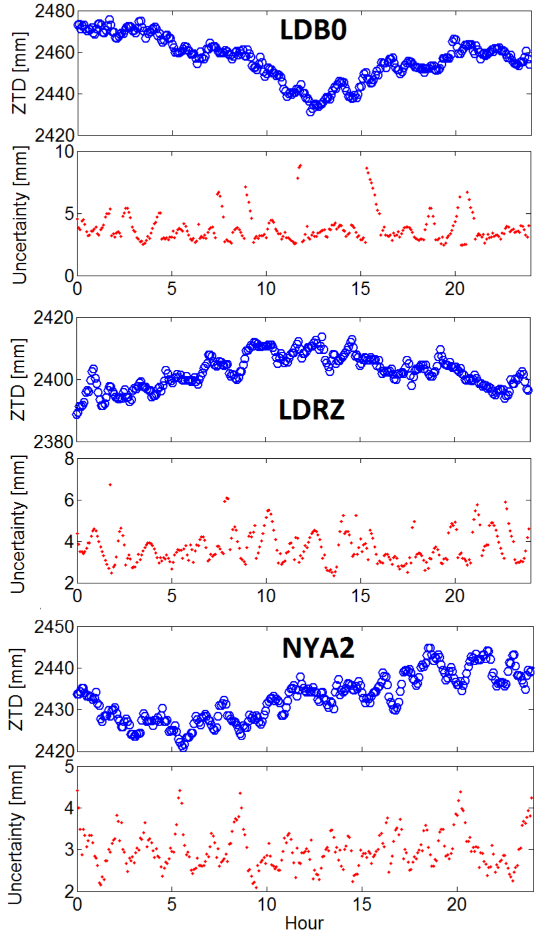

Figure 5. The time series of the estimated ZTD and the corresponding total ZTD uncertainty, for one day (1 June 2014) and for the three GRUAN sites: LDB0, LDRZ and NYA2.

AMTD
8, 8817–8857, 2015

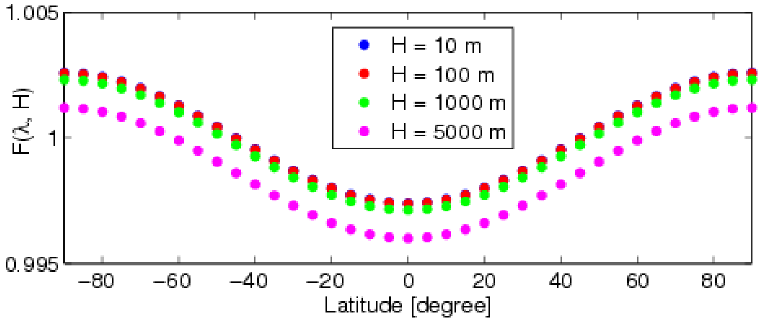

Figure 6. Values of $f(\lambda, H)$ calculated from different latitudes and from four different site heights.

AMTD
8, 8817–8857, 2015

The uncertainty of the GNSS-derived IWV

T. Ning et al.

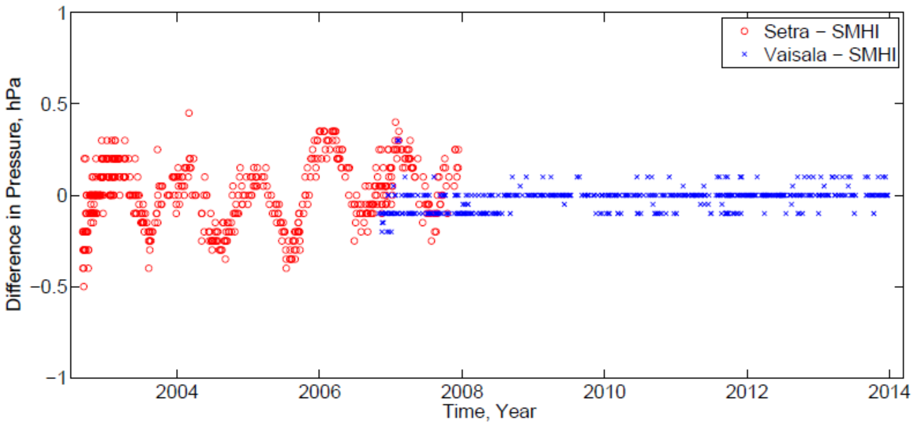

Figure 7. Differences in the surface pressure measured by three different barometers.

AMTD
8, 8817–8857, 2015

The uncertainty of the GNSS-derived IWV

T. Ning et al.

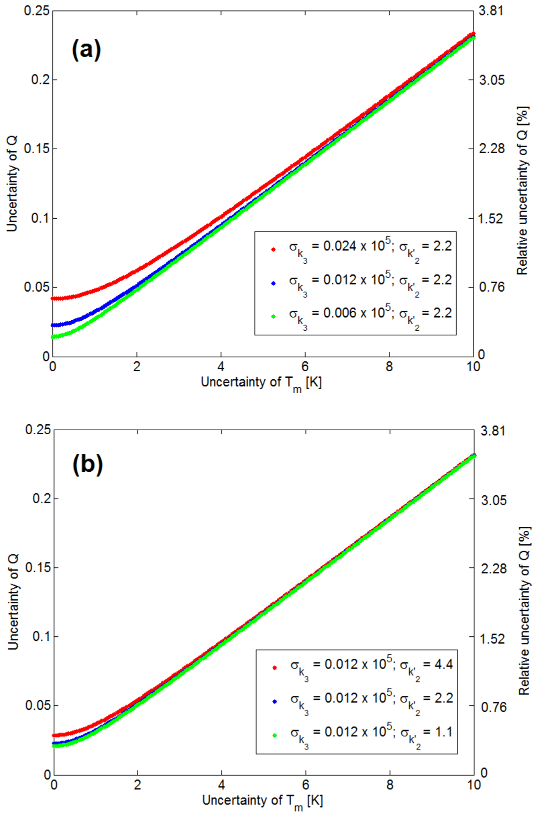

Figure 8. The uncertainty of the conversion factor Q as a function of the uncertainty in the mean temperature (T_m) and for three groups of the uncertainties in the constants k_3 and k_2': the nominal value (blue line), the double of the nominal value (red line), and the half of the nominal value (green line) for **(a)** a fixed uncertainty of k_2' and **(b)** a fixed uncertainty of k_3.

AMTD
8, 8817–8857, 2015

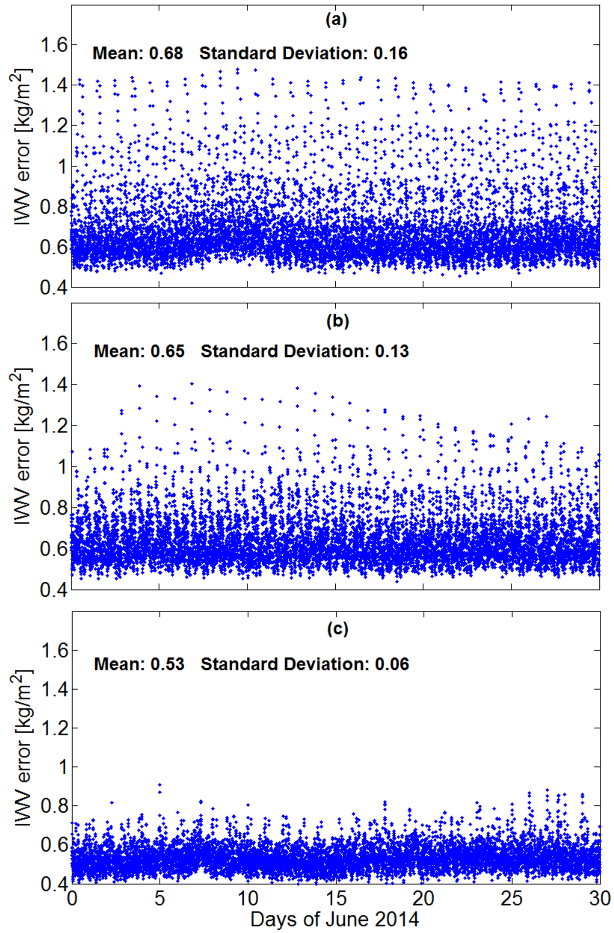

Figure 9. The estimated total IWV uncertainty for the month of June, 2014 and for three GRUAN sites: **(a)** LDB0, **(b)** LDRZ and **(c)** NYA2.

AMTD
8, 8817–8857, 2015

The uncertainty of the GNSS-derived IWV

T. Ning et al.

Title Page
Abstract Introduction
Conclusions References
Tables Figures
◀ ▶
Back Close
Full Screen / Esc
Printer-friendly Version
Interactive Discussion